SSRG International Journal of Electrical and Electronics Engineering
ISSN: 2348-8379/ https://doi.org/10.14445/23488379/IJEEE-V11I1P104

Volume 11 Issue 1, 28-45, January 2024

Original Article

An Innovative Closed Loop Control Approach with High Gain Improved SEPIC-Luo Converter for PV-Powered PMBLDC Motor

S. Prakash[1], K. Boopathy[2]

[1,2]*Department of Electrical and Electronics Engineering, Aarupadai Veedu Institute of Technology, Vinayaka Missions Research Foundation, Tamilnadu, India.*

[1]*Corresponding Author : prakash.yours@gmail.com*

Received: 15 October 2023 Revised: 17 November 2023 Accepted: 14 December 2023 Published: 20 January 2024

Abstract *- This work mainly focuses on affording a consistent and unceasing power supply to a three-phase Permanent Magnet Brushless DC (PMBLDC) motor. The solar array serves as a power generation component in this case. Owing to the inconsistent nature of the PV panel, the output is relatively low, a high gain improved Single Ended Primary Inductance Converter (SEPIC) integrated Luo converter is implemented to maximize the voltage generated by the solar panel. The acquired DC output voltage from the converter is stabilized using a Proportional Integral (PI) controller based on an innovative hybrid Improved Whale Optimization assisted Bat Algorithm (IWO-BA) is proposed. This optimization performs an automatic updating of controller parameters while keeping the voltage stable. The primary switching frequency of the Voltage Source Inverter (VSI) is produced by electronic communication in the PMBLDC motor. As thus, VSI losses caused by a high switching frequency are reduced. The PI controller controls PMBLDC motor speed by sensing the precise position of the rotor and comparing it with the reference speed. The control of a Three-Phase Voltage Source Inverter (3ϕVSI) connected to the grid is accomplished by expanding a PI-supported Hysteresis Current Controller (HCC). Finally, the steady power is delivered to the three-phase PMBLDC motor without any distortions. MATLAB platform simulation is utilized to ensure the entire effectiveness of the proposed work. From the results obtained, it is evident that the proposed system achieves the highest efficiency value of 99.1% with a minimized THD value of 1.21%.*

Keywords *- PV system, PMBLDC motor, IWO-BA optimized PI controller, 3ϕVSI, HCC.*

1. Introduction

People are turning more and more towards the usage of green energy sources as a result of population growth and global warming, which is fast depleting conventional energy supplies [1]. PV modules are widely employed in a variety of applications, including standalone or grid-interactive systems [2, 3]. The solar energy is transformed into DC power by the PV system. The temperature, cloud cover and intensity of the atmosphere all have an impact on the photovoltaic array's production [4]. It needs the assistance of a DC-DC converter to raise its low panel voltage prior to being linked to a load or grid to achieve the required voltage level [5, 6].

The operational point lies at the junction of the cell's volt-ampere properties and the load, which is linked across the cell. PMBLDC motors are usually powered by a three-phase or single-phase voltage source inverter circuit in conjunction with a DC-DC converter from an AC main supply [7]. According to its voltage gain, the basic DC-DC Boost converter is capable of increasing voltage continuously [8].

Conversely, its boosting ability is limited when used in high-gain applications because of conduction losses, and parasitic resistances. According to this, the internal susceptibility of the inductor limits the gain of the Buck-Boost converter at high-duty cycles [9, 10].

Novel converter topologies are presented in order to mitigate the shortcomings of primary converters. Converters such as Cuk, Zeta, and SEPIC are based on the Buck-Boost converter topology. The Cuk converter displays inverted output voltage polarity even though it has the least amount of current ripple [11, 12]. Operating at comparatively lower ON time than OFF time, the SEPIC converter may offer high voltage gain, and have a positive output voltage polarity [13, 14]. The Zeta converter receives the Buck-Boost converter's discontinuous input current as a disadvantage, but the input current of the other two converters is continuous [7, 15].

By adding more diodes, capacitors, or inductors, the increasing factor constraint that impacts the effectiveness of

all of the above mentioned converters is primarily addressed. Therefore, a unique high gain improved SEPIC integrated Luo converter is proposed in this research by combining two distinct converters, namely the Luo converter, and the SEPIC converter. It is possible to lower ripple current, and voltage at the output side with this proposed converter.

Furthermore, a control mechanism is essential to guarantee that the converter's output continues to operate at a constant voltage. To improve the overall performance, the system control approach needs to be implemented several research studies have been published, but these approaches have suffered due to some limitations, which are discussed below.

To achieve a steady-state operation in the converter, a control strategy utilizing the PI controller is implemented [16]. Concerns like peak overshoot lead to the development of optimization-based techniques. The load's nonlinearity, and dynamic fluctuation are increased by the traditional PI controller. In light of this, the PI controller is used in conjunction with the latest optimization tools, Genetic Algorithm (GA) [17], Grey Wolf Optimization (GWO) [19], Particle Swarm Optimisation (PSO) [18], and Ant Colony Optimization (ACO) [20] techniques, to quickly provide an intended result.

These methods, however, have a low rate of convergence during the iterative process and are prone to local optimum collapse in high-dimensional spaces. Thereby, this work introduces the novel hybrid Improved Whale-Bat algorithm to address the abovementioned challenges. The goal of this work is to reduce the oscillatory current in the motor, increase energy efficiency in PMBLDC motors, and solve commutation issues inside the motor. Furthermore, while the PV-fed PMBLDC motor operates independently and interactively with the grid, the power quality is thus preserved. The proposed work's objectives are listed below:

- A closed-loop PI controller governs the speed control of the PMBLDC motor. Commutation is implemented on the PI controller because it offers more freedom, and resources for implementing control algorithms.
- A high gain improved SEPIC-Luo is achieved for successful voltage boosting, combined with the use of a hybrid IWO-Bat algorithm technique, resulting in a stable DC link voltage with minimal power losses.
- To establish a grid-interactive system that provides power at night, and endorses extra solar power during the day.
- To reduce the grid current's THD below less than 5%.

The remainder of this work is summarised below: section 2 shows the proposed system description; section 3 discusses the phases of the proposed system in detail; and section 4 shows the findings of the comparison evaluation. Finally, section 5 provides a conclusion of the work.

2. Proposed System Description

This paper highlights a PMBLDC motor drive that enables the use of a solar Photovoltaic (PV) array, and grid. With the goal of optimizing solar PV-generated power using an efficient control scheme technique, solar PV array-fed drive systems normally require a DC-to-DC converter stage. Figure 1 illustrates the proposed PV-powered PMBLDC motor using high gain improved SEPIC-Luo converter with a tuned PI controller.

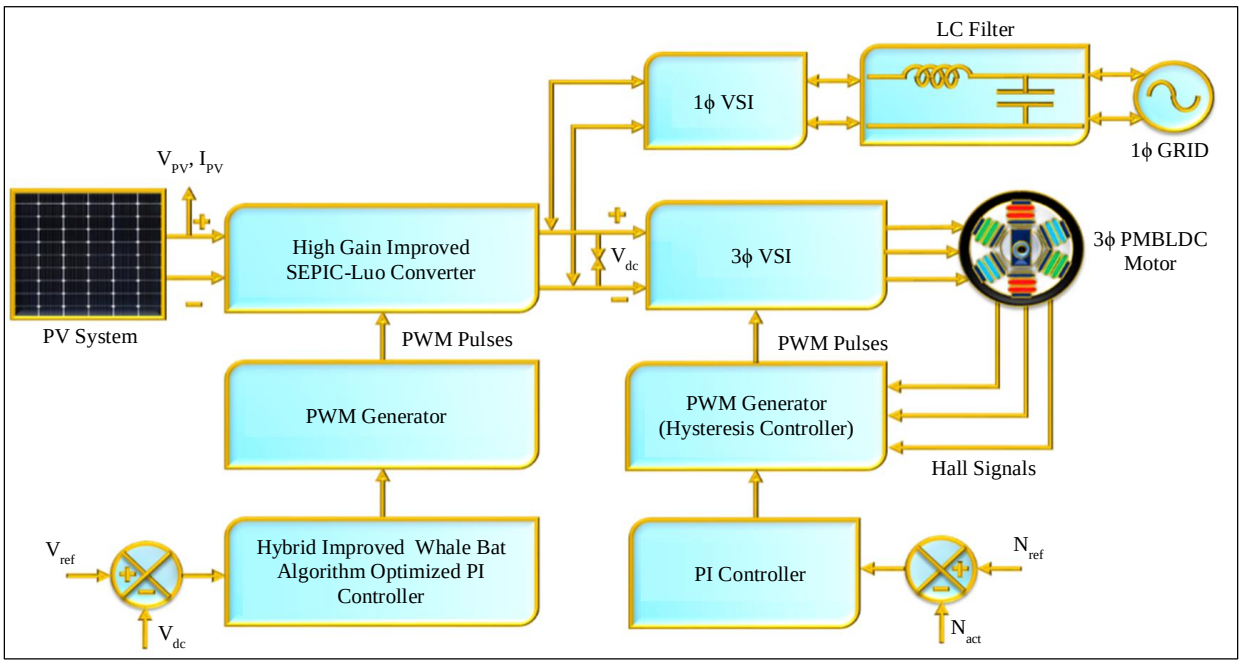

Fig. 1 PV system-based PMBLDC motor using hybrid improved whale-bat tuned PI controller

In this proposed study, the high-gain improved SEPIC integrated Luo converter is employed to enlarge the resultant voltage attained from a PV system. Following that, the reference voltage (V_{ref}) is analogized to the DC real voltage (V_{dc}), resulting in an error signal that is sent to an optimization-based PI controller. The hybrid improved whale with bat algorithm optimized PI controller is deployed to regulate the proposed converter, and mitigate for erroneous signals precisely. The regulated output is sent to the PWM generator, which is capable of producing pulses that ensure the converter functions smoothly.

Furthermore, the DC link voltage is given to a three-phase VSI for converting the DC-AC supply. In addition, the actual speed N_{act} is analogized with the reference speed N_{ref}, which produces the error signal and is subjected to hysteresis current controller assisted PI controller for producing control signal with error compensation. The HCC controller regulates electrical load current by constraining it to adhere to a fixed value. It is accomplished through the inverter's switching action, which preserves the current within the hysteresis band.

The required pulses for the superior operation of the inverter are attained by adopting the PWM generator. Here, the PI controller is deployed to govern the consistent speed of the PMBLDC motor. The PMBLDC motor utilizes the grid power via 1ϕVSI whenever the PV power output is inadequate for operating the motor. Finally, the proposed approach provides an uninterruptible and continuous power supply free of harmonics to the PMBLDC motor application.

3. Proposed System Modelling

3.1. Modelling PV System

PV-based power plants are emerging as significant sources of clean energy due to their advantages over other forms of renewable power, including no fuel requirement, zero pollution, minimal upkeep, and reduced noise. The equivalent solar energy system circuitry schematic is shown in Figure 2. Following is an equation connecting the PV panel's voltage, and current.

$$V_{PV} = n_S \frac{AKT}{q} In\left\{\frac{n_p I_{SC} - I_{PV} + n_p I_o}{n_p I_o}\right\} - \frac{n_S}{n_p} I_{PV} R_S \quad (1)$$

$$P_{PV} = V_{PV} * I_{PV} \quad (2)$$

Each parameter has an MPP at which the PV system is able to function efficiently. The effectiveness of the PV array is shown in Figure 3.

It is necessary to use an appropriate DC to DC converter to achieve the desired dc output voltage from a PV panel. In this work, the high gain improved SEPIC-Luo converter is used to obtain a higher gain DC output voltage. In addition, the working operation of the proposed converter is discussed in the below section.

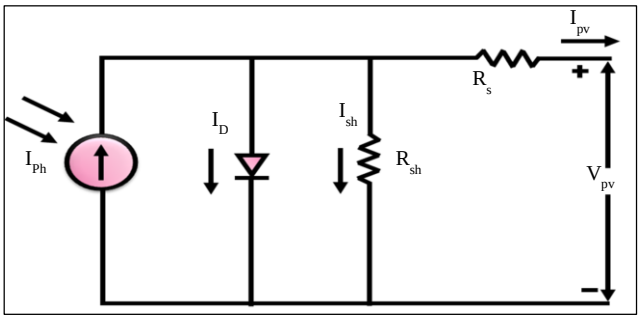

Fig. 2 Circuit diagram of PV

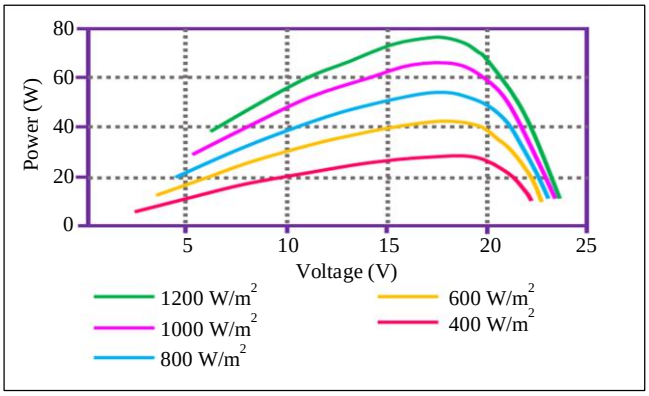

Fig. 3 PV system performance at T=25°C

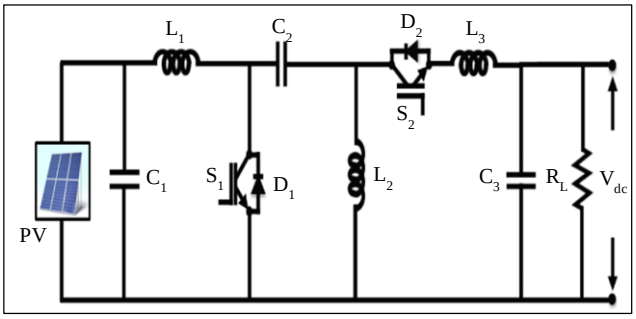

Fig. 4 High gain improved SEPIC - Luo converter

3.2. Modelling of High Gain Improved SEPIC Integrated LUO Converter

In the past decade, Distributed Energy Sources (DES) such as PV and wind energy systems have had a massive influence by satisfying the expanding power demand while also meeting rigorous environmental pollution standards. Overall, the PV panel produces a low voltage (in the 12 to 60 V range) at its output. According to the recognized limitations of series-linked PV structures, the optimum solution to meet the load voltage requirement is a high-gain DC to DC converter. Therefore, this work proposes a high-gain, improved SEPIC - Luo converter to fulfil the load demand efficiently. Here, the obtained PV output is boosted with reduced ripples through the use of the proposed converter, which incorporates the benefits of both SEPIC, and Luo. Figure 4 illustrates the equivalent circuit diagram of high gain improved SEPIC integrated Luo converter.

Stage 1 : In stage I, only a PV source is available to generate power to meet a load demand. SEPIC converter boosts the voltage when the switch S_1 is on, and diode D_1 is on and switch S_2 is off, diode D_2 is off. During the period stage 1, shown in Figure 5(a) L_1 is charged by a PV source, the capacitors C_1 starts discharging the stored energy to the inductor L_2.

$$I_{L1} = I_{PV} + \frac{I_{L1}}{L_1} t \quad (3)$$

$$I_{L2} = I_{dc} + \frac{I_{c1}}{L_2} t \quad (4)$$

$$I_{L3} = I_{dc} + \frac{I_{c2}}{L_3} t \quad (5)$$

The mathematical equations of inductor currents L_1, L_2, and L_3 are shown in Equations (3), (4), and (5) respectively.

Stage 2 : In stage II, only a PV source is available for power generation. The Luo converter bucks the voltage down when the switch S_2 is on, and diode D_2 is on, and switch S_1 is off, diode D_1 is off. During the period stage 2, as shown in Figure 5(b), L_2 is charged by the PV source, and the L_1 is charged by the capacitors C_1. D_1 provides the closed path to charge the L_2, L_3 by discharging the capacitor C_3.

$$I_{L1} = V_{PV} - \frac{V_{c1}}{L_1} t + I_{PV} \quad (6)$$

$$I_{L2} = I_{dc} - \frac{V_{c3}}{L_2} t \quad (7)$$

$$I_{L3} = I_{dc} - \frac{I_{c2}}{L_3} t \quad (8)$$

The mathematical equations of inductor currents L_1, L_2, and L_3 are shown in Equations (6), (7), and (8) respectively. The conceptual waveforms of the proposed converter are depicted in Figure 6. The operation of the converter is further improved with the aid of an improved PI controller, and this work uses a hybrid IW-bat algorithm to change the parameters of the PI controller.

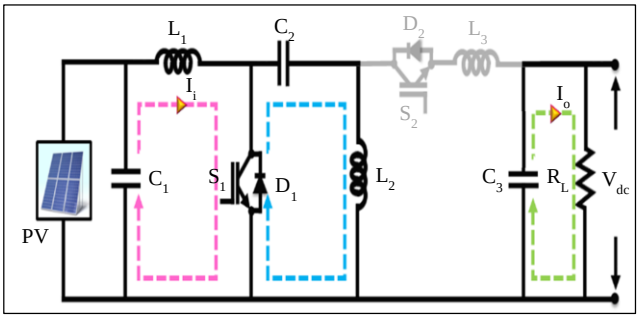

Fig. 5(a) Stage I

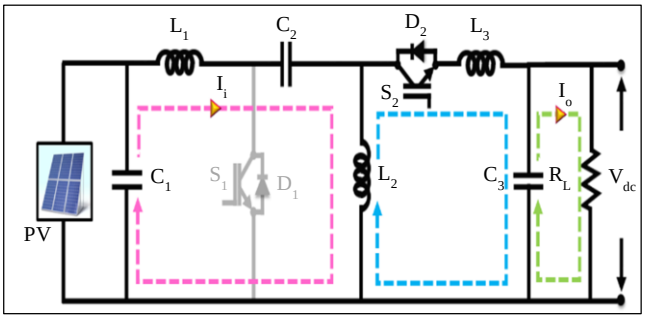

Fig. 5(b) Stage II

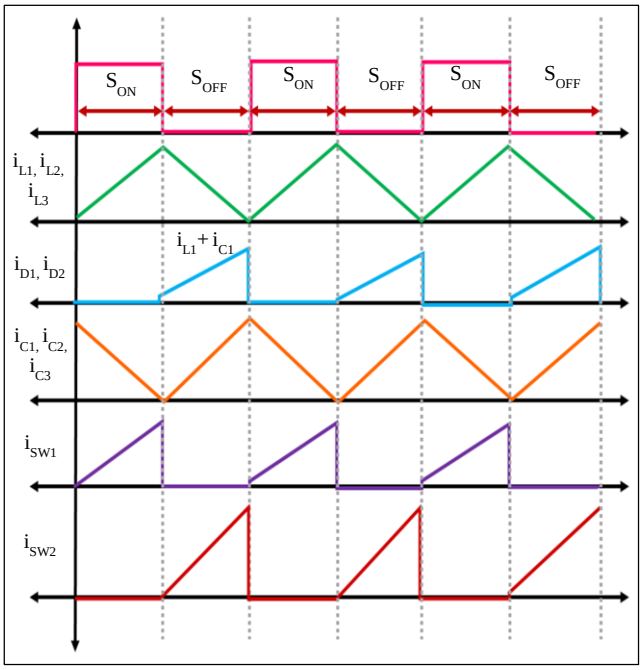

Fig. 6 Characteristics waveform of the proposed converter

3.3. Modelling of Hybrid Improved Whale-Bat Algorithm Optimized PI Controller

The hybrid optimized PI controller is employed in this research to enlarge the converter function's performance. Compared to proportional action alone, the PI controller has disadvantages such as a more significant maximum deviation, a longer response time, and a more extended oscillation period. The hybrid IWO-Bat algorithm is suggested as a response to optimize the PI controller. With regard to convergence precision and rate, the IWOA performs well. When handling complicated problems, it also faces the issue of producing a local best solution. Therefore, to address the challenges mentioned above, a Bat algorithm is adopted with IWOA.

3.3.1. PI Controller

An established controller with the ability to retain precise set points is called a PI controller. Proportional and integral control modes are combined to form the foundation of the PI controller's functional modelling. From the k_p, and k_i

parameters, the logical equation for the PI controller may be obtained. Equation (9), which describes the typical form of a PI controller, calls. k_i the integral gain, and k_P is the proportional gain.

$$u(t) = k_P e(t) + k_i \int e(t)dt \quad (9)$$

Using the Laplace transform, Equation (10) is changed to Equation (11),

$$U(s) = k_P E(s) + \frac{k_i E(s)}{s} \quad (10)$$

PI regarding the time constraints is expressed in Equation (10),

$$U(s) = k_P[1 + \frac{1}{\tau_i}]E(s) \quad (11)$$

Where, $k_i = \frac{k_P}{\tau_i}$ and $k_P = k_d/\tau_i$

The steady-state error of the model is decreased, and the proportional and integral terms more finely control an error signal. When $k_P$and k_i parameters are precisely tuned for a closed-loop control system, the settling time improves, and the rise time somewhat decreases. A number of software-based ideas have been implemented to support controller tuning. The primary output of the work is optimization; to enhance control performance, the PI controller has recently been implemented.

3.3.2. Hybrid Improved Whale–Bat Algorithm

The whale optimization algorithm replicates the foraging habits of humpback whales. The following phases comprise the algorithm: encircling the target, bubbling the net and attacking it, and pointing for the prey**.**

1. Encircling stage of prey: Assuming that the dimensions of the searching space are d, and the whale population scale is N, the expression for whale individual i is $Xi = (xi\ 1, xi\ 2, \ldots, xi\ d)$, where $i = 1, 2, \ldots, N$. The location of the prey lines up with the objective function's global optimal solution. Consequently, the following is an expression of the mathematical model of the surrounding prey stage.

$$D = |C.X_P(t) - X(t)| \quad (12)$$

$$X(t+1) = X_P(t) - A.D \quad (13)$$

Where t is the number of current iterations, X (t) is the location vector of the whale individual, and $X_P(t)$ is the current optimal solution. D is the distance vector between the seeking current, and individual optimal solution. One can compute the coefficient vectors A, and C using,

$$A = 2a.r_1 - a \quad (14)$$

$$C = 2.r_2 \quad (15)$$

Where a continuously diminishes from 2 to 0 with t's increase, and r_1, and r_2 are random vectors in [0, 1]:

$$a(t) = 2\left(1 - \frac{t}{t_{max}}\right) \quad (16)$$

2. The stage of bubbling-net attacks: During this phase, the whale initiates a spiral movement around its current victim in order to get closer to it. The spiral motion's calculated model is as follows:

$$X(t+1) = D'.e^{bi}.cos(2\pi l) + X_P(t)(p > 0.5) \quad (17)$$

Where, b defines the form of the logarithmic spiral, l is a random number in $[-1,1]$, and $D' = |X_P(t) - X(t)|$ is the distance vector between the searching individual, and the current optimal solution. The likelihood variable p in $[0,1]$ is utilized to synchronize the behaviours of bubbling-net attack, and encircling prey. As a result, the calculated model may be expressed as follows:

$$X(t+1) = \begin{cases} X_P(t) - A.D(p < 0.5) \\ D'.e^{bi.cos(2\pi l) + X_{P(t)}}(p > 0.5) \end{cases} \quad (18)$$

3. The stage of hunting for prey. Based on the value of $|A|$, the whale individual determines whether to circle or look for prey. The whale is unable to precisely pinpoint the location of the prey when $|A| > 1$. As a result, it is required to select a random person to serve as the prey, that is:

$$D'' = |C.X_{rand} - X|, \quad (19)$$

$$X(t+1) = X_{rand} - A.D'' \quad (20)$$

3.3.3. Improved Method of WO

1. The strategy of tent mapping. Because the typical WOA uses the random approach to create its initial population, it may have little variety. Tent mapping, a novel chaotic mapping technique, has been thus used. First, tent mapping using the equation can be used to create the chaotic sequence $y = \{yd, d = 1, 2, \ldots, d\}, yd = \{yid, i = 1, 2, \ldots, N\}$ for a dimension d, and population scale N .

$$y_{i+1,d} = \begin{cases} 2y_{id}, y_{id}, < 0.5 \\ 2(1 - y_{id}), y_{id} \geq 0.5 \end{cases} \quad (21)$$

By projecting the chaotic sequence to an appropriate space, one can derive a population $X = \{Xi, i = 1, 2, \ldots, N\}$, and Xi = $\{X_{id}, d = 1, 2, \ldots, d\}$.

$$X_{id} = X_{min.d} + y_{id}(X_{max.d} - X_{min.d}) \quad (22)$$

Where, the top, and lower bounds of X_{id} are correspondingly represented by $X_{max.d}, and\ X_{min.d}$. Then, in accordance with X, the reverse population OX can be derived by,

$$OX_{id} = X_{max.d} + X_{min.d} - X_{id} \quad (23)$$

Finally, combine population $X, and\ OX$. Then, order the resulting population based on the fitness of the objective function; the top N people can be considered the original population.

2. The nonlinear convergence factor, and self-adaptive weighting strategy: In typical WOA, the linear decrease of the convergence factor cannot coordinate the local exploitation, and global searching. As a result, it is preferable to decrease a downward speed of a with the number of iterations t. The nonlinear convergence factor equation is,

$$a = 2\left[1 - cos(\mu \frac{t}{t_{max}}\pi + \theta)\right] \quad (24)$$

The self-adaptive weight technique with the nonlinear convergence factor. The traditional WOA's linear decline of convergence factor is unable to synchronize both local exploitation, and worldwide searching. As a result, it is preferable to achieve a decrease in speed as the number of repetitions increases(t). The nonlinear convergence factor equation that has been suggested is,

$$\omega(t) = 1 - \frac{e^{t/t_{max}-1}}{e-1} \quad (25)$$

Then Equations (13), and (17) are changed into,

$$X_{(t+1)} = \omega(t).X_P(t) - A.D \quad (26)$$

$$X(t+1) = D'.e^{bi}.cos(2\pi l) + \omega(t).X_P(t)(P > 0.5) \quad (27)$$

3. An approach for diversity variety: With the standard WOA iterative procedure, the population's diversity will gradually decline, perhaps causing the algorithm to converge prematurely. As a result, when the diversity is less than the threshold value, it is necessary to do a different procedure for the population. If individual *I* has a fitness value of f_i, then the minimum, maximum and mean values of the current population are, respectively, $f_{max}, f_{min},$ and f_{mean}. The present variation in population is then,

$$\sigma^2 = \frac{1}{N}\sum_{i=1}^{n}(\frac{f_i - f_{mean}}{f_{max} - f_{min}})^2 \quad (28)$$

The variation operation is carried out in the following ways while the variance is less than the threshold value:

$$X(t+1) = r_3.[X_P(t) - (t)] + r_4.[X'(t) - X(t)] \quad (29)$$

Where, $X'(t)$ is a randomly selected member of the population, and r_3, and r_4 are random values in [0,1].

It is possible to simulate the movement, attitude, and swarm behaviour of bats in the searching process of whales using basic mathematical equations, as is discussed in this section. Initially, three additional parameters need to be created in order to describe bat movement:

- Frequency of pulse $Q_i^{(t)}$,
- Velocity $V_i^{(t)}$, and
- Position $X_i^{(t+1)}$,

Where, $X_i^{(t+1)}$ is the position of the $i-th$ bat at generation t, $V_i^{(t)}$is the velocity of a single bat, and $Q_i^{(t)}$ is the actual pulse frequency. A bat's flight is summed up by using Equations 30–32:

$$Q_i^{(t)} = Q_{min}^{(t)} + (Q_{max}^{(t)} - Q_{min}^{(t)}.\beta_i \quad (30)$$

$$V_i^{(t)} = V_i^{(t)} + \left[X_i^{(t)} - X_{best}^{(t)}\right].Q_i \quad (31)$$

$$X_i^{(t)} = X_i^{(t)} + V_i^{(t)} \quad (32)$$

The range of the output pulse frequency is $Q_i^{(t)} \epsilon [Q_{min}, Q_{max}]$. The output pulse is specified by the random number $\beta \epsilon [0,1]$, and the optimal solution as of just now is best presented by $X_{best}^{(t)}$. Using two exploration strategies, and parameter $r_i^{(t)}$, the exploration and exploitation elements that comprise the search process are balanced in the BA. More exploratory is the first exploration approach represented by Equation 32, whereas the second strategy is written as,

$$X_{new} = X_{old} + \epsilon.\overline{A}^{(t)} \quad (33)$$

Performs the random walk, a form of local search that is more concerned with making use of the best solution at the moment. Observe that, if appropriate, the new best solution in the Equation is represented by X_{new}The best solution at present is represented by xold. $\overline{A}^{(t)}$is the average loudness, and $\epsilon$is the randomized integer in range (-1, 1).

The final tactic is used in accordance with the pulse rate $r_i^{(t)}$. Throughout generations, the pulse rate has typically varied to mimic the natural behaviour of bats, which emit loud pulses with low pulse rates when hunting and silent pulses with high pulse rates when approaching their prey. The proposed hybrid IWO-BA algorithm flowchart is represented in Figure 7.

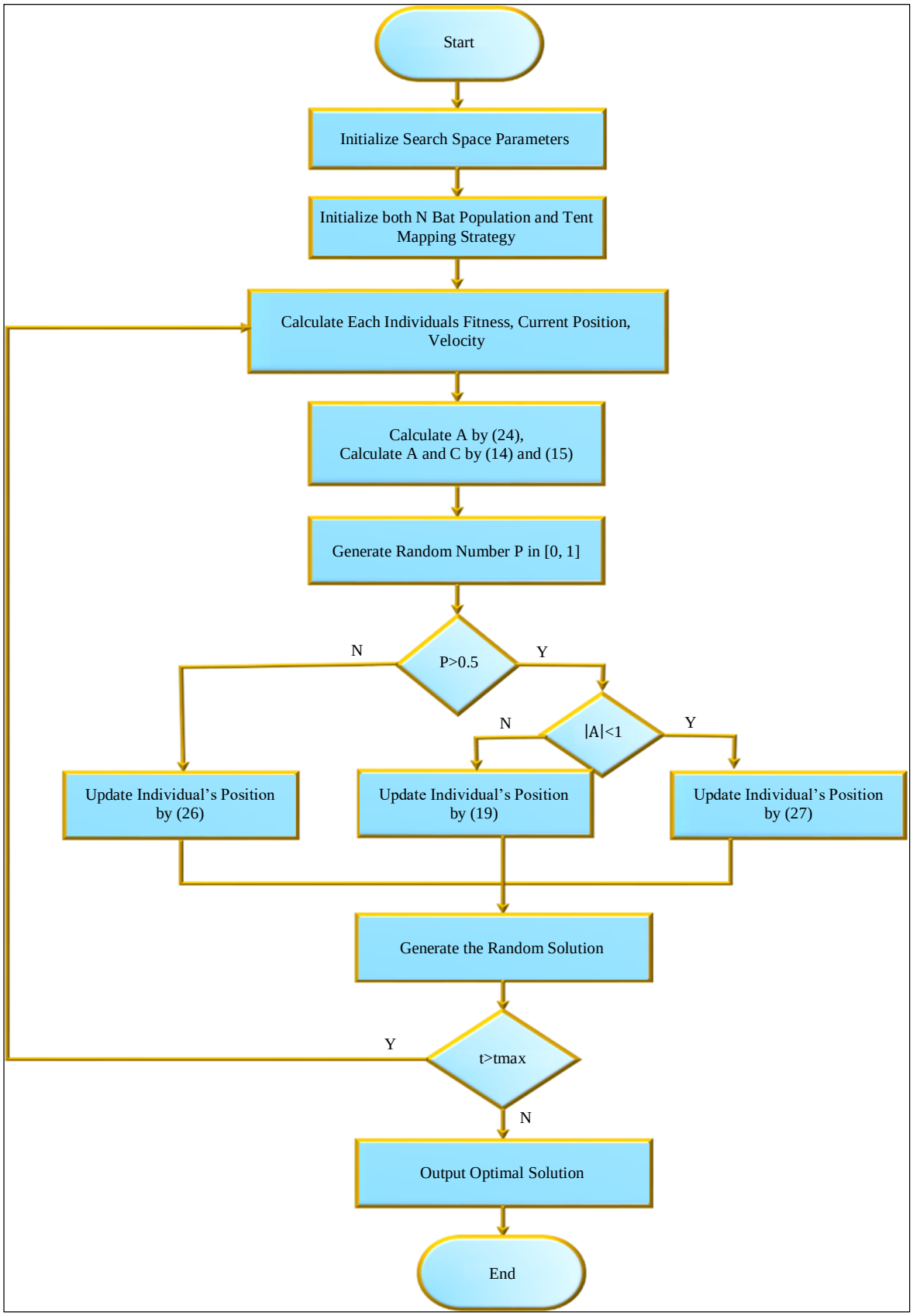

Fig. 7 Hybrid IWO-Bat algorithm

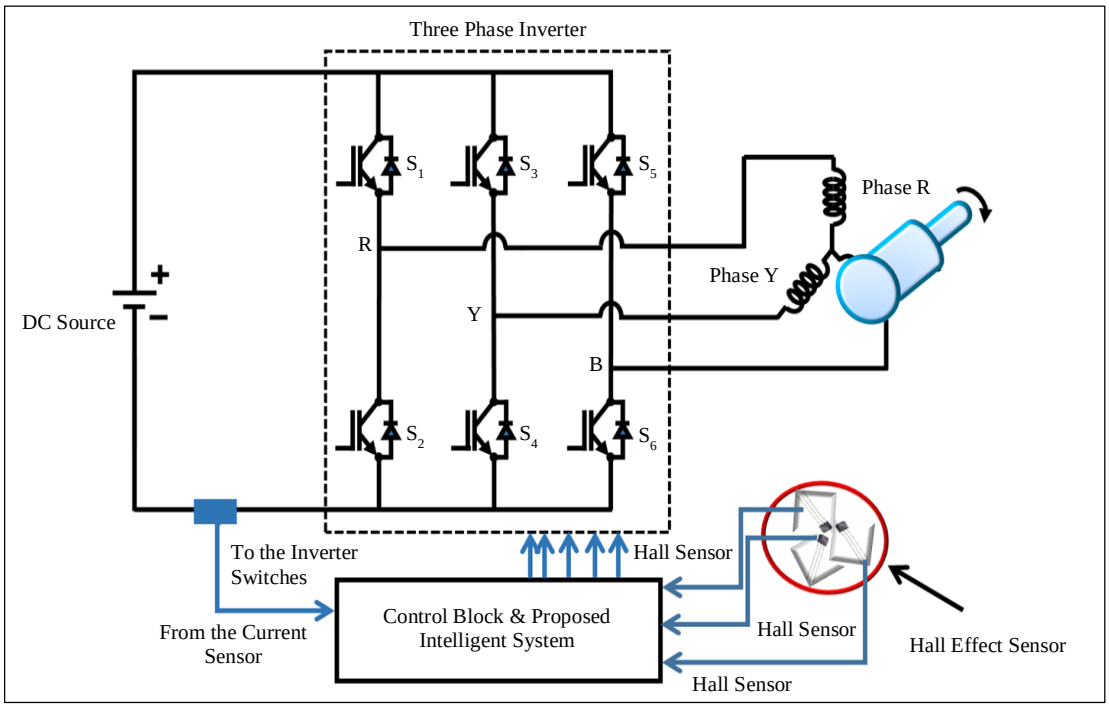

Fig. 8 PMBLDC motor equivalent circuit

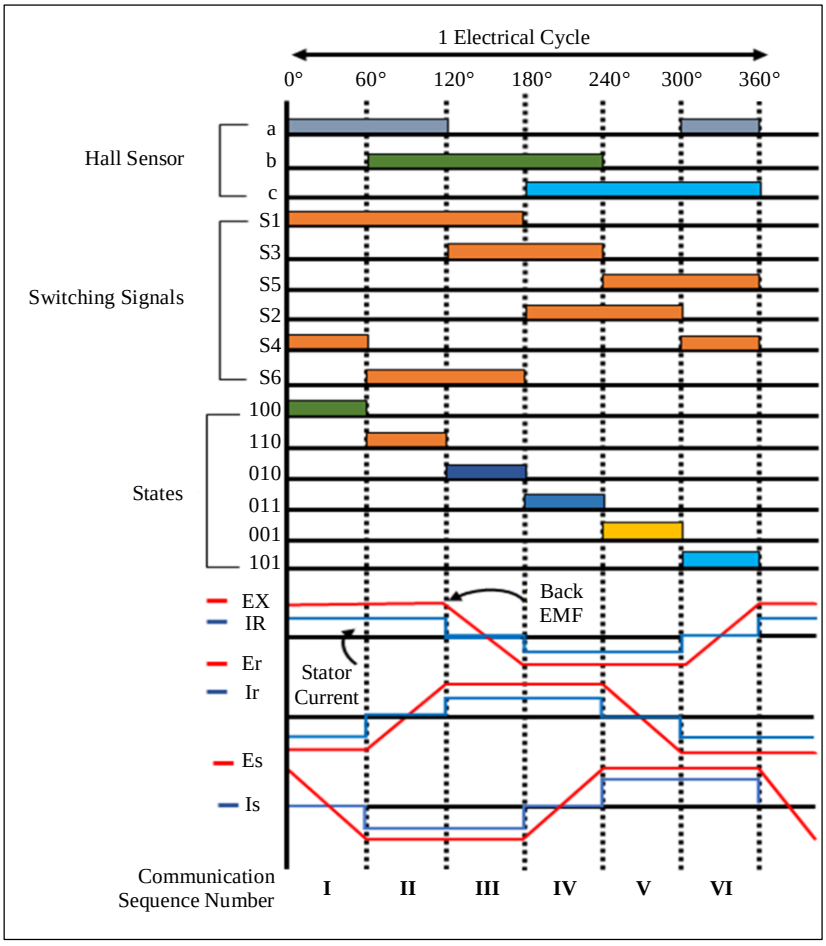

Fig. 9 Waveforms of armature current, switching signals, back EMFs, and hall sensor signals

Table 1. Six states of hall sensors

States	Hall A	Hall B	Hall C	Switches to be ON	Stator Winding Active Lines
I	1	0	0	S1, S4	RY
II	1	1	0	S1, S6	RB
III	0	1	0	S3, S6	YB
IV	0	1	1	S3, S2	YR
V	0	0	1	S5, S2	BR
VI	1	0	1	S5, S4	BY

3.4. Modelling of PMBLDC Motor

The components of a PMBLDC drive are a control system, driver circuit, inverter circuit (including solid state switches), and DC power supply. A PMBLDC motor drive system's general layout is depicted in Figure 8. Figure 8 shows that the position of the rotor, and present feedback signal for torque computation is obtained by the control system using three digital signals obtained from hall sensors.

The inverter's upper side switches ($S_1, S_3,$ and S_5), and lower side switches ($S_2, S_4,$ and S_6) are shown in Figure 8. The three-phase lines R, Y, and B as well as the gate pulses produced by the control block, activate these switches in response to the commutation signals received from the position sensors. In the driving mode of the BLDC motor, the switching signals, switching sequences, and hall sensor signals are displayed in Figure 9.

The phase armature back EMFs in Figure 9. $E_R, E_B,$ and I_R are represented by the corresponding currents, $I_Y, I_B,$ and I_R. According to Figure 9, there are six states associated with the three position sensors, and their associated active switches. The hysteresis current controller produces the inverter's switching signals by comparing the i_{abc} at the inverter output with the i_{abc}^* reference current generated at the control unit's input. PI effectively regulates the PMBLDC motor speed-assisted HCC controller, which is explained in the following section.

3.5. Hysteresis Current Controller

A PMBLDC motor with a hysteresis current controller is presented in Figure 10. Control speed of the motor is done by a PI-type speed controller in this system. When the hall sensor outputs are converted into three-phase signals positioned 120 degrees apart by a commutator logic decoder, the corresponding stator current signal waveforms are generated by the commutator logic decoder. The speed control system output represents the peak currents of the three reference stators. In hysteresis current controllers, the stator currents are controlled within a specific acceptable band. Switching impulses are obtained by semiconductor transistors of three-phase VSI inverters by analyzing the resulting signals of power controllers.

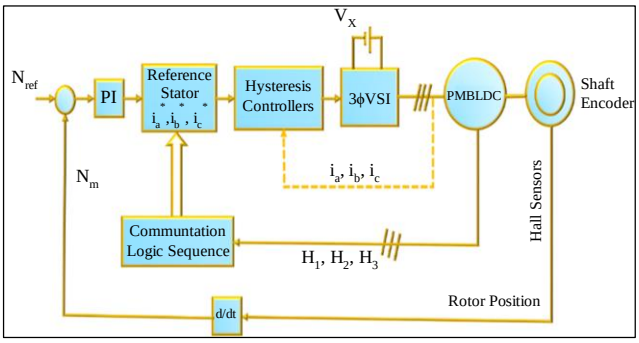

Fig. 10 Hysteresis current controller

Table 2. Parameter description

Parameters	Values
Short Circuit Current	8.3A
Peak Power	10KW, 10 panels
Open Circuit Voltage	12V
Number of Cells Connected in Series N_s	36
High Gain Improved SEPIC-Luo Converter	
Switching Frequency	10KHz
L_1, L_2, L_3	1.3mH
C_1, C_2	22µF
C_3	2200µF
Diode	MCD95
BLDC Motor	
Speed	30000 rpm
Load Inertia (J)	9 x 10^{-4} Nm^2

4. Results and Discussion

In the present research, a highly efficient DC-DC converter based on solar systems is proposed as a consistent power source for PMBLDC-driven systems. The output voltage becomes stronger with fewer switching losses by integrating the high-gain improved SEPIC- Luo converter. Moreover, the controlled output voltage is reached by using a hybrid IW-Bat algorithm-optimized PI controller. MATLAB / Simulink is utilized to carry out the proposed approach with the goal of demonstrating the efficacy of the research work.

As a result, as shown in the following illustration, the developed method provides high efficiency, fast convergence, and reduced THD. The proposed model's parameter specification is shown in Table 2. The waveforms for irradiation, voltage, current, and temperature in solar PV panels are shown in Figure 11. Temperature variation is included as an operating condition in order to analyze how well the provided methodology overcomes the nonlinear behaviour of the PV system. The temperature is raised to 30°C after it is continuously maintained at 25°C till 0.25 seconds; similarly, the PV panel irradiation varies from 800 w/sq.m to 1000 w/sq.m.

Waveforms show the way temperature change affects things. The PV voltage increases in proportion to the temperature change, from an initial magnitude of 48V to 56V. Likewise, at 0.25 s, the PV current stabilized 11A with minor distortions. Figure 12 demonstrates the output current and voltage waveforms of the proposed high-gain improved SEPIC-Luo converter. From the waveform observation, it is clear that the use proposed IWO-BA tuned PI controller efficiently maintains the constant voltage 300V after 0.1 seconds.

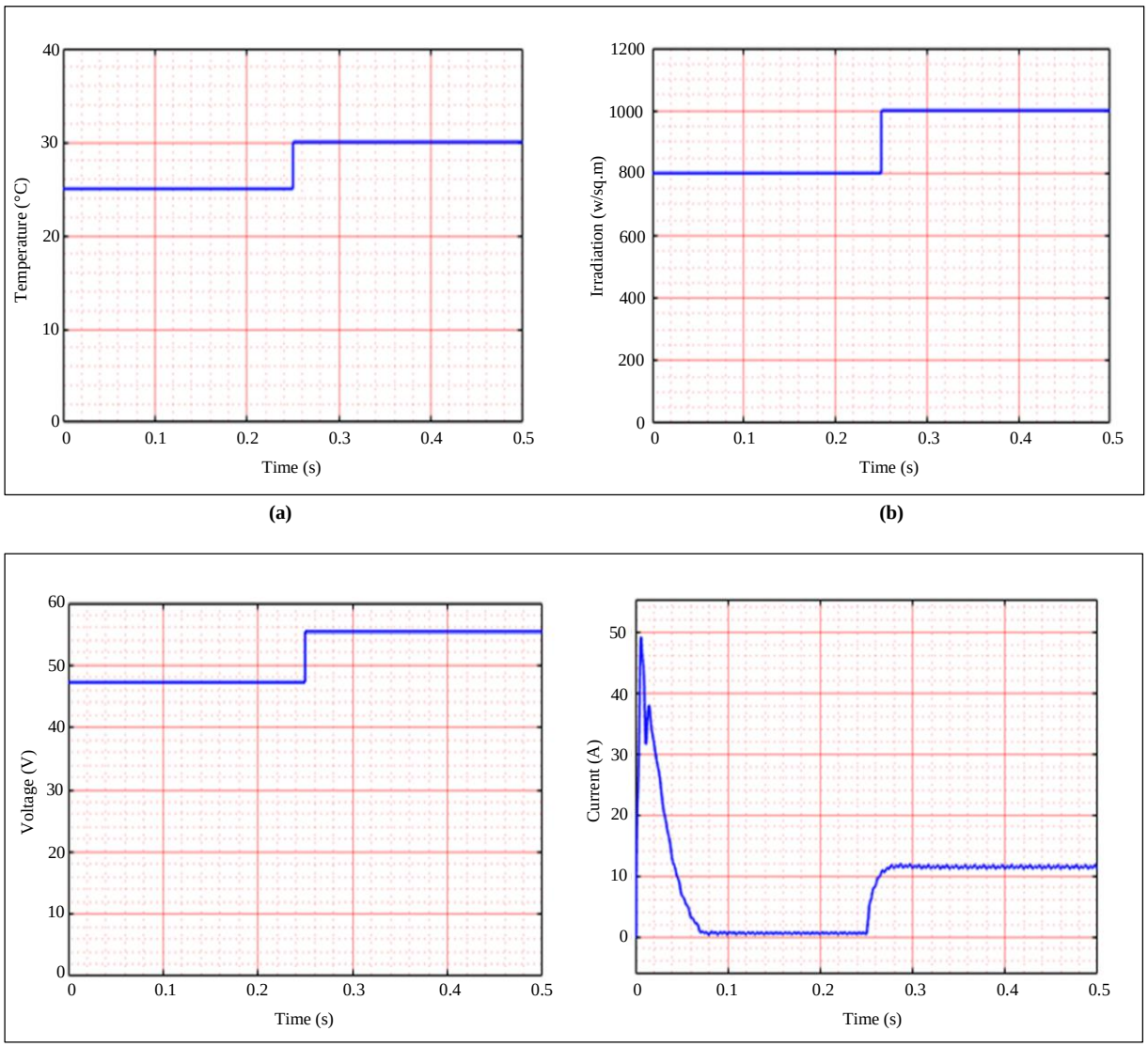

(a) **(b)** **(c)** **(d)**

Fig. 11 Output waveforms of PV panel (a) Temparature, (b) Irradiation, (c) Voltage, and (d) Current.

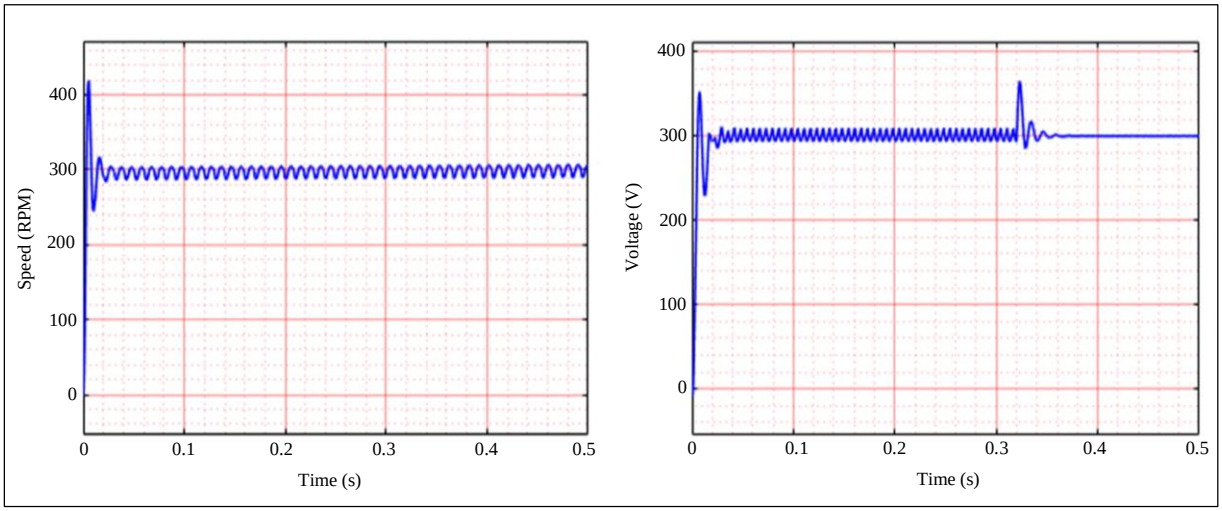

(a) **(b)**

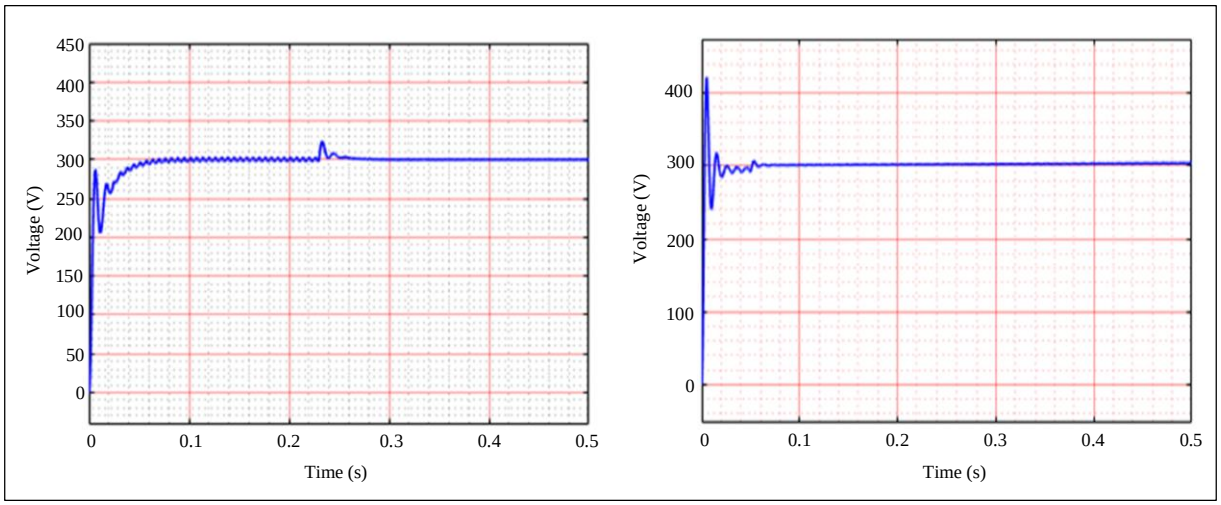

(c) **(d)**

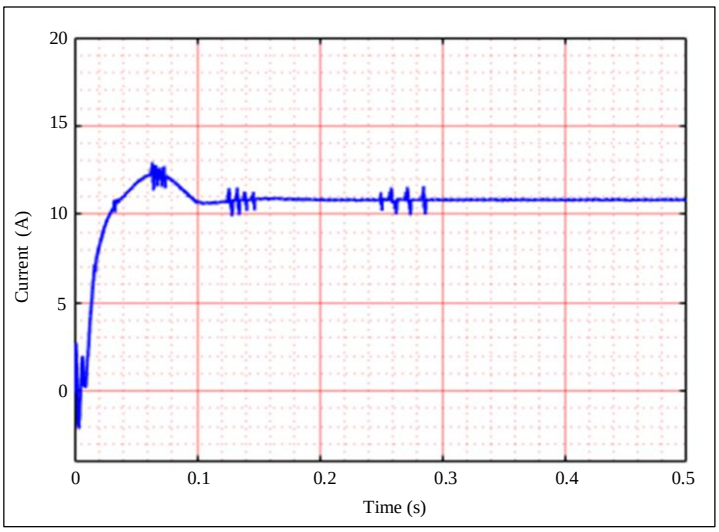

(e)

Fig. 12 Output waveforms of high gain improved SEPIC-Luo converter voltage using (a) PI controller, (b) GWO-PI, (c) Bat-PI, (d) Hybrid IWO-BA tuned PI controller, and (e) Converter current.

Furthermore, when compared to other controller approaches, including conventional PI, GWO-PI and Bat-PI controllers, the proposed optimized PI controller is superior with regard to fast settling time, which is (t_s = 0.1 sec). Similarly, the current becomes stable with a small amount of distortions after 3.5 seconds.

4.1. At No Load Condition

The obtained output waveforms of the BLDC motor at no load condition are illustrated in Figure 13. Under the no-load condition, the PMBLDC motor maintains the constant 1000 rpm after 0.1 secs; similarly, it is typically measured in units of newton-meters per ampere (Nm/A) and the BLDC motor torque is determined by the number of windings in stator, the number of magnets in the rotor, and the size, and shape of the magnets.

4.2. At Load 1 NM

The BLDC motor's torque, speed, back emf, and current waveforms are displayed in Figure 14. The PMBLDC motor's performance under 1 Nm speed circumstances is examined using the waveforms mentioned above. The motor accelerates at first, and then steadily to a steady speed of 1000 rpm in 0.3 seconds. The motor's torque, back emf, and current waveforms all show the effects of speed fluctuation. The PMBLDC motor current keeps the 3A consistent output at 0.3 seconds. Likewise, the motor torque rises sharply from 0 to 9 Nm in 0.05 seconds, and then rapidly returns to 1 Nm. The motor's rear emf rises at a rate of 0.05 seconds as it goes from -48 to 48 V.

4.3. At Load 2 NM

The waveforms shown in Figure 15 are utilized to examine the operation of a PMBLDC motor under 2 Nm speed instances. After 0.3 seconds, the motor's speed gradually climbs to a constant speed of 1000 rpm. Similarly, the motor torque increases abruptly from 0 to 8 Nm at 0.05 s before immediately returning to 2 Nm. Similarly, the output load waveform of the BLDC motor maintains 2 Nm after 0.3 sec.

4.4. At Load 3 NM

The waveforms illustrated in Figure 16 serve to investigate the behaviour of a PMBLDC motor at 3 Nm speed conditions. The motor's speed steadily increases to a constant speed of 1000 rpm after 0.3 seconds. Similarly, the motor torque jumps rapidly from 0 to 8 Nm in 0.05 s before returning to 3 Nm immediately. Similarly, the BLDC motor's output load waveform remains 3 Nm after 0.3 sec.

Figure 17 depicts the grid's current, voltage, reactive, and real power output waveforms. According to the observations, the constant grid voltage of 230V is maintained, and the grid current waveform becomes constant after 0.05 sec at 5A. Real power reaches a stable value, and reactive power is zero. Figure 18 shows the proposed converter achieving a THD value of 1.21% by eliminating harmonics.

The proposed system's efficiency, and THD comparative study are shown in Figures 19, and 20. The proposed system's efficiency comparison is given in Table 3, and THD comparison is given in Table 4. It is evident from the graph analysis that the proposed approach outperforms other prevalent methods with regard to an efficiency value of 99.1%, and a THD value of 1.21%.

Table 5 shows the PI controller with an optimized PI controller comparison. Comparing the proposed hybrid IWO-BA optimized PI controller to conventional PI, GWO-tuned PI, and BA-tuned PI controllers, it achieves a speedy 0.1s settling time.

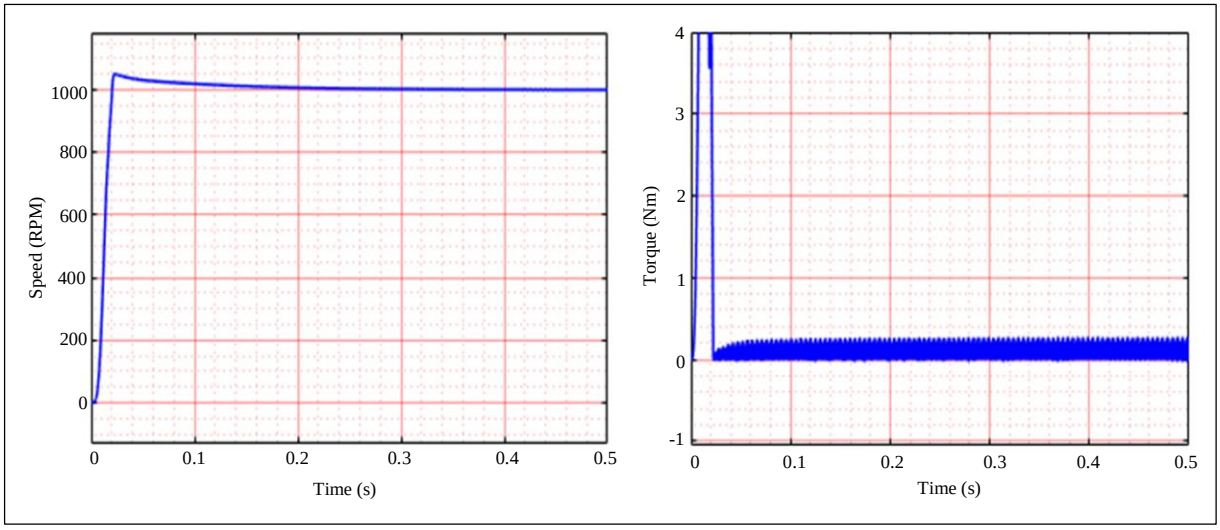

(a) **(b)**

Fig. 13 Output waveforms of BLDC motor at no load condition (a) Motor speed, and (b) Motor torque.

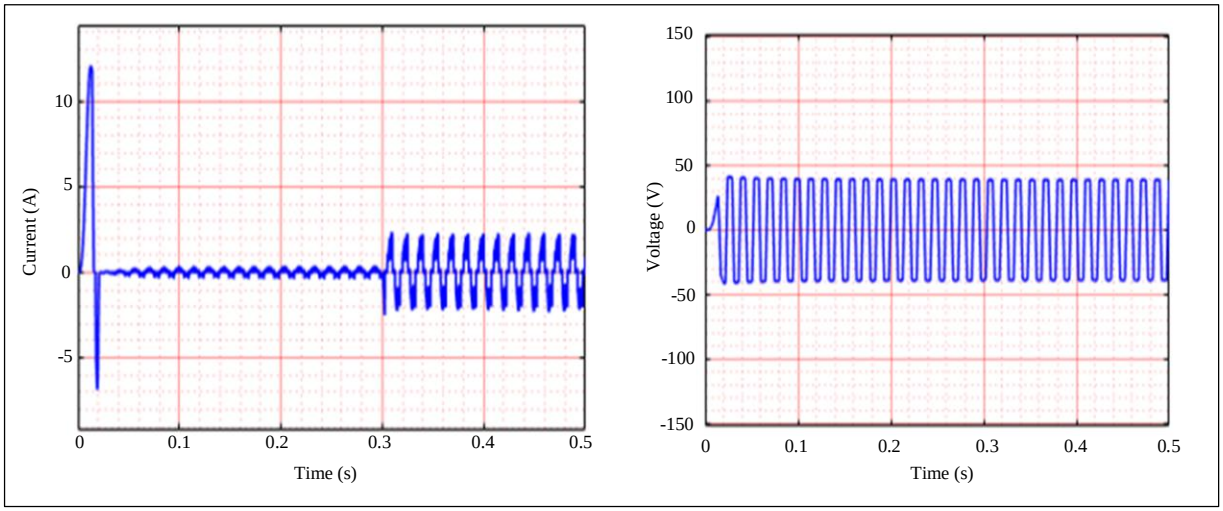

(a) **(b)**

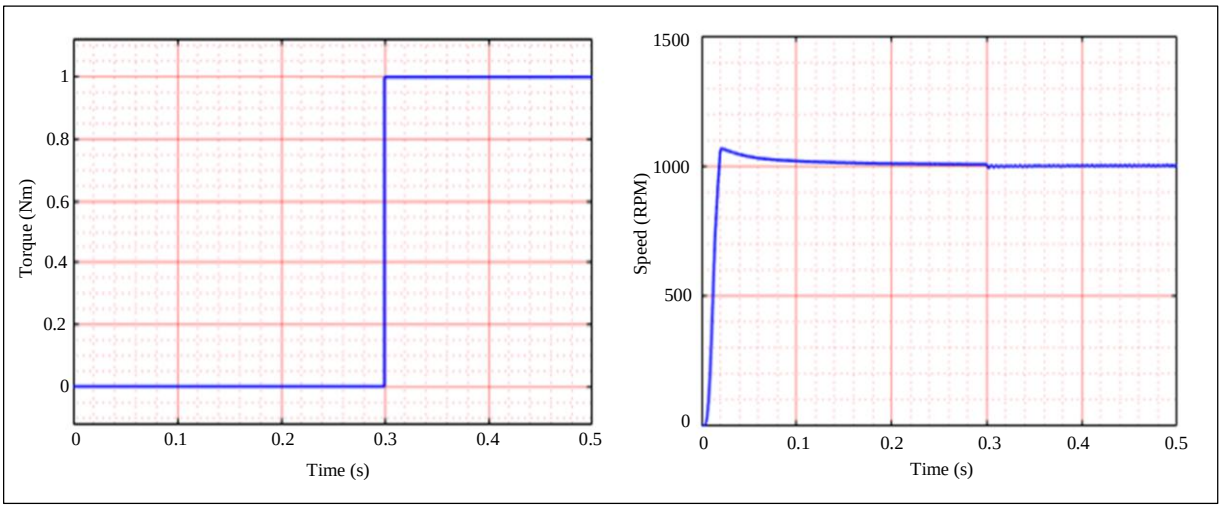

(c) **(d)**

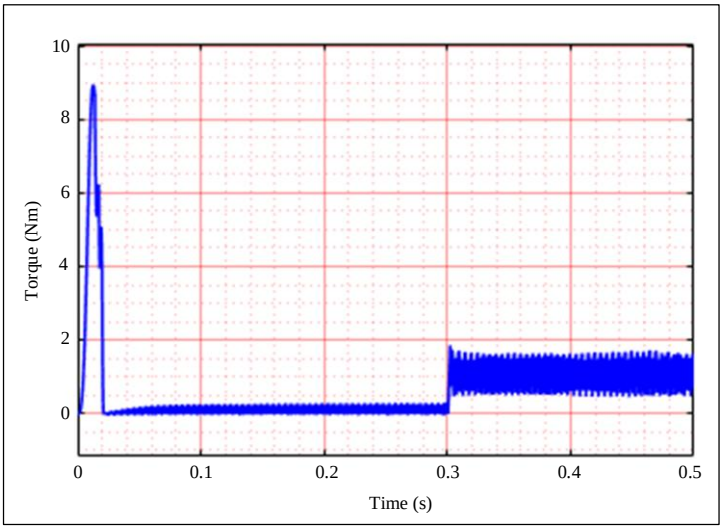

(e)

Fig. 14 Output waveforms of BLDC motor at no 1 Nm condition (a) Motor current, (b) Back EMF, (c) Load, (d) Motor speed, and (e) Motor torque.

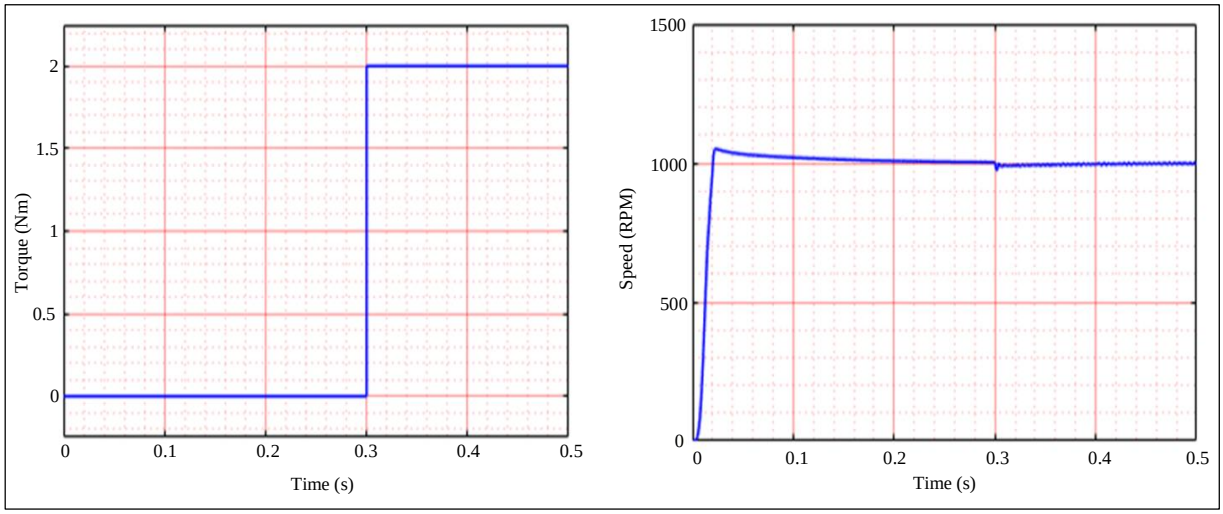

(a) **(b)**

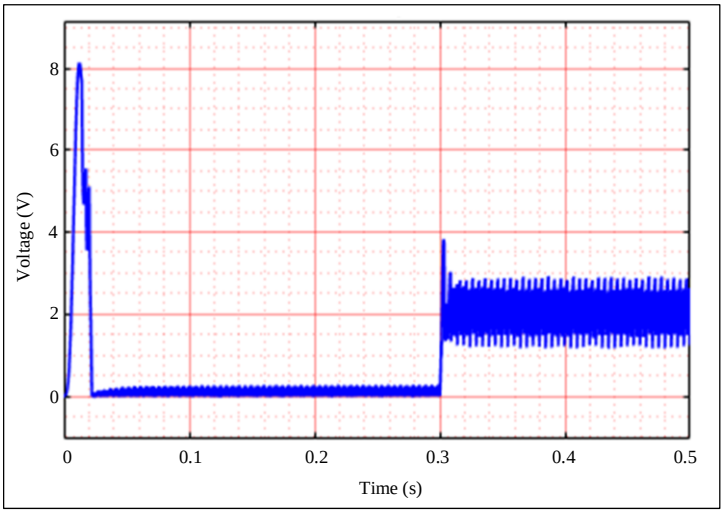

(c)

Fig. 15 Output waveforms of BLDC motor at no 2 Nm condition (a) Load, (b) Motor speed, and (c) Motor torque.

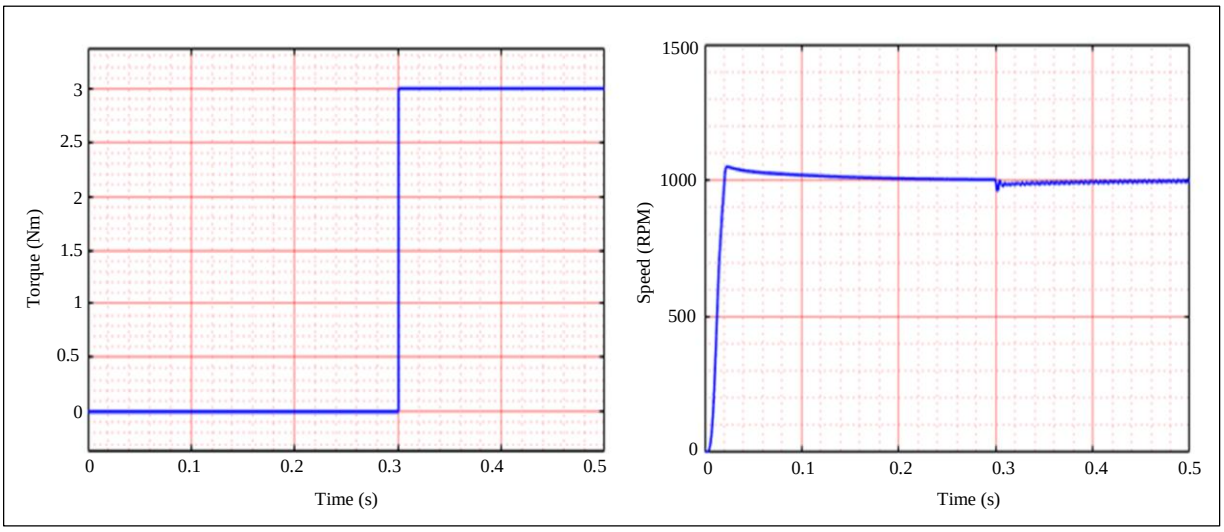

(a) **(b)**

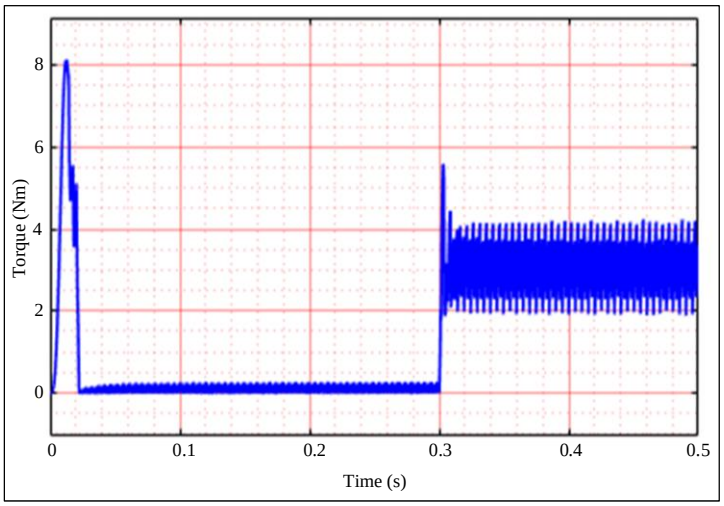

(c)

Fig. 16 Output waveforms of BLDC motor at no 3 Nm condition (a) Load, (b) Motor speed, and (c) Motor torque.

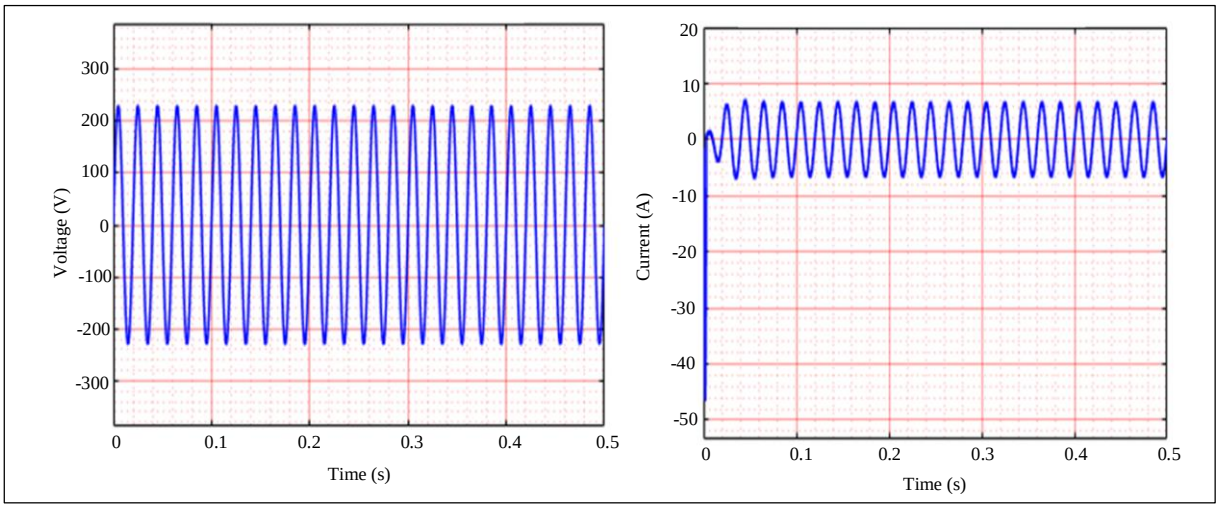

(a) **(b)**

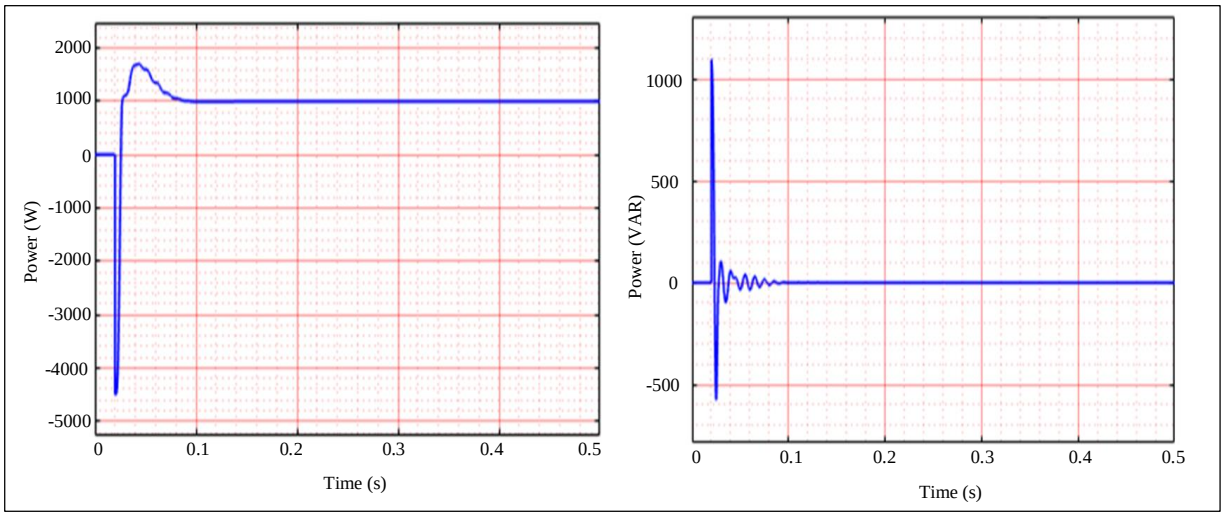

(c) **(d)**

Fig. 17 Output waveforms of grid side (a) Voltage, (b) Current, (c) Real power, and (d) Reactive power.

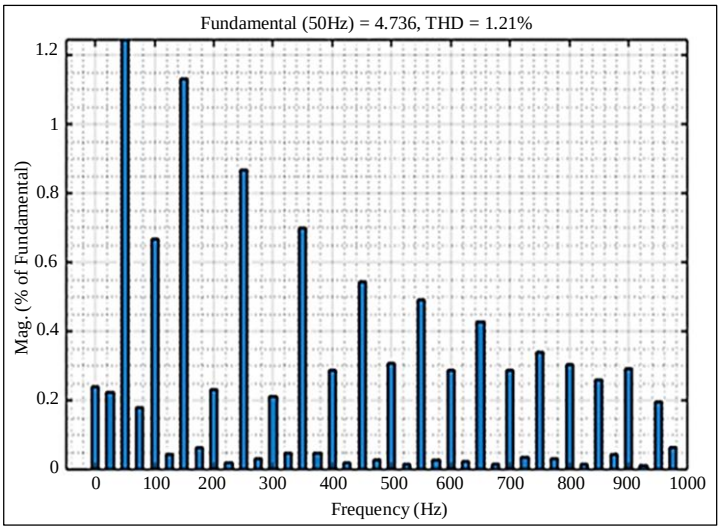

Fig. 18 THD waveform

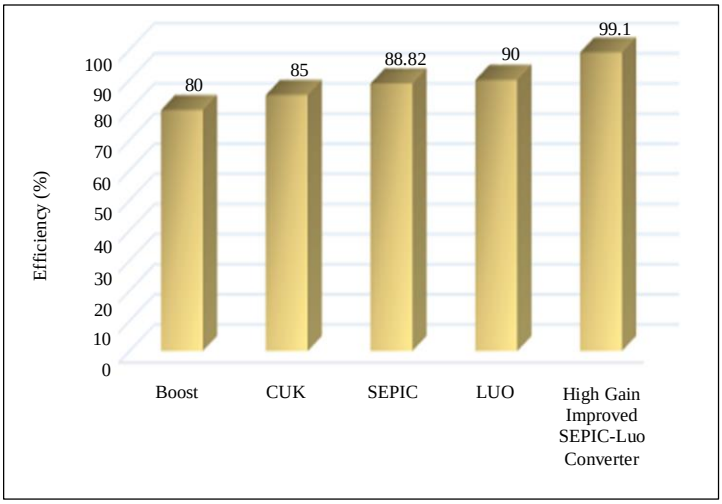

Fig. 19 Efficiency comparison

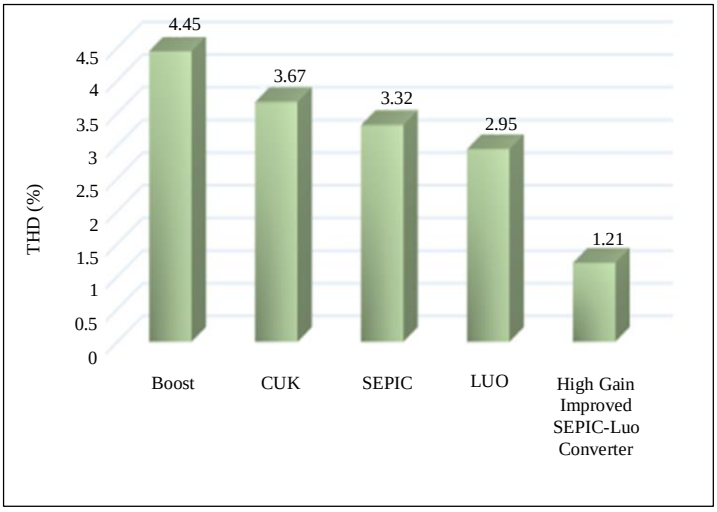

Fig. 20 THD comparison

Table 3. Efficiency comparison

Converters	Efficiency (%)
Boost	80 [21]
Cuk	85 [22]
SEPIC	88.82 [23]
LUO	90 [24]
Proposed High Gain Improved SEPIC-Luo Converter	99.1

Table 4. THD comparison

Converters	THD (%)
Boost	4.45
Cuk	3.67
SEPIC	3.32
Luo	2.95
Proposed High Gain Improved SEPIC-Luo Converter	1.21

Table 5. Comparison of controller dynamic response

Controller	Parameters		
	Rise Time (t_r)	Peak Time (t_p)	Settling Time (t_s)
PI	0.01 s	0.02 s	-
GWO-PI	0.01 s	0.02s	0.35 s
BA-PI	0.01 s	0.02s	0.25 s
Hybrid IWO-BA-PI	0.01 s	0.01 s	0.1 s

5. Conclusion

The main goal of this work is to enable a three-phase PMBLDC motor to receive a steady, and uninterrupted power supply. In this instance, the PV array functions as a power generation unit. Because photovoltaic panels fluctuate, their output is relatively modest, and their gain is high. The SEPIC-Luo converter has been enhanced in order to optimize the voltage produced by the solar panel. A PI controller built on the cutting-edge Hybrid IWO-BA technique stabilizes the obtained DC output voltage from the converter. By measuring the exact rotor position and comparing it to reference speed with actual speed, the PI controller controls the speed of the PMBLDC motor. A PI-enabled HCC controller is utilized to regulate the three-phase VSI linked to the grid. Ultimately, the three-phase PMBLDC motor receives a distortion-free supply of constant power. The proposed architecture is entirely specific to be effective by using MATLAB platform simulation. The results clearly show that the proposed system has the lowest THD value of 1.21%, and the highest efficiency value of 99.1%.

References

[1] K.S. Kavin, and P. SubhaKaruvelam, "PV-Based Grid Interactive PMBLDC Electric Vehicle with High Gain Interleaved DC-DC SEPIC Converter," *IETE Journal of Research*, vol. 69, no. 7, pp. 4791-4805, 2021. [CrossRef] [Google Scholar] [Publisher Link]

[2] Rajan Kumar, and Bhim Singh, "Grid Interactive Solar PV-Based Water Pumping Using BLDC Motor Drive," *IEEE Transactions on Industry Applications*, vol. 55, no. 5, pp. 5153-5165, 2019. [CrossRef] [Google Scholar] [Publisher Link]

[3] A. Darcy Gnana Jegha et al., "A High Gain DC-DC Converter with Grey Wolf Optimizer Based MPPT Algorithm for PV Fed BLDC Motor Drive," *Applied Sciences*, vol. 10, no. 8, pp. 1-20, 2020. [CrossRef] [Google Scholar] [Publisher Link]

[4] S. Sashidhar, V. Guru Prasad Reddy, and B.G. Fernandes, "A Single-Stage Sensorless Control of a PV-Based Bore-Well Submersible BLDC Motor," *IEEE Journal of Emerging and Selected Topics in Power Electronics*, vol. 7, no. 2, pp. 1173-1180, 2018. [CrossRef] [Google Scholar] [Publisher Link]

[5] Jun Cai et al., "An Integrated Power Converter-Based Brushless DC Motor Drive System," *IEEE Transactions on Power Electronics*, vol. 37, no. 7, pp. 8322-8332, 2022. [CrossRef] [Google Scholar] [Publisher Link]

[6] Sariki Murali, Kaibalya Prasad Panda, and Gayadhar Panda, "PV-HESS Fed BLDC Driven Water Pumping System with PSO-Based MPP Tracking Employing Zeta Converter," *2018 IEEE Innovative Smart Grid Technologies-Asia (ISGT Asia)*, Singapore, pp. 196-201, 2018. [CrossRef] [Google Scholar] [Publisher Link]

[7] Rohini Diofode, and Jayesh Suryawanshi, "Control of BLDC Motor Using PV Fed Bridgeless Single Switch SEPIC Converter," *International Journal of Innovative Technology and Exploring Engineering*, vol. 9, no. 1, pp. 2575-2580, 2019. [CrossRef] [Google Scholar] [Publisher Link]

[8] Abdelkhalek Chellakhi, Said El Beid, and Younes Abouelmahjoub, "An advanced MPPT Scheme for PV Systems Application with Less Output Ripple Magnitude of the Boost Converter," *International Journal of Photoenergy*, vol. 2022, pp. 1-21, 2022. [CrossRef] [Google Scholar] [Publisher Link]

[9] Niraj Rana, and Subrata Banerjee, "Development of an Improved Input-Parallel Output-Series Buck-Boost Converter and Its Closed-Loop Control," *IEEE Transactions on Industrial Electronics*, vol. 67, no. 8, pp. 6428-6438, 2020. [CrossRef] [Google Scholar] [Publisher Link]

[10] Ramón Silva-Ortigoza et al., "Robust Flatness Tracking Control for the 'DC/DC Buck Converter-DC Motor' System: Renewable Energy-Based Power Supply," *Complexity*, vol. 2021, pp. 1-18, 2021. [CrossRef] [Google Scholar] [Publisher Link]

[11] Julio Cezar dos Santos de Morais, Juliano Luiz dos Santos de Morais, and Roger Gules, "Photovoltaic AC Module Based on a Cuk Converter with a Switched-Inductor Structure," *IEEE Transactions on Industrial Electronics*, vol. 66, no. 5, pp. 3881-3890, 2019. [CrossRef] [Google Scholar] [Publisher Link]

[12] Kuditi Kamalapathi et al., "A Hybrid Moth-Flame Fuzzy Logic Controller Based Integrated Cuk Converter Fed Brushless DC Motor for Power Factor Correction," *Electronics*, vol. 7, no. 11, pp. 1-19, 2018. [CrossRef] [Google Scholar] [Publisher Link]

[13] Kok Soon Tey et al., "Improved Differential Evolution-Based MPPT Algorithm Using SEPIC for PV Systems under Partial Shading Conditions and Load Variation," *IEEE Transactions on Industrial Informatics*, vol. 14, no. 10, pp. 4322-4333, 2018. [CrossRef] [Google Scholar] [Publisher Link]

[14] Selvarani Natchimuthu, Muniraj Chinnusamy, and Arul Prasanna Mark, "Experimental Investigation of PV Based Modified SEPIC Converter Fed Hybrid Electric Vehicle (PV-HEV)," *International Journal of Circuit Theory and Applications*, vol. 48, no. 6, pp. 980-996, 2020. [CrossRef] [Google Scholar] [Publisher Link]

[15] Akhil Raj, Sabha Raj Arya, and Jyoti Gupta, "Solar PV Array-Based DC–DC Converter with MPPT for Low Power Applications," *Renewable Energy Focus*, vol. 34, pp. 109-119, 2020. [CrossRef] [Google Scholar] [Publisher Link]

[16] Fahd A. Alturki et al., "Novel Manta Rays Foraging Optimization Algorithm Based Optimal Control for Grid-Connected PV Energy System," *IEEE Access*, vol. 8, pp. 187276-187290, 2020. [CrossRef] [Google Scholar] [Publisher Link]

[17] Subbiah Durgadevi, and Mallapu Gopinath Umamaheswari, "Analysis and Design of Single Phase Power Factor Correction with DC–DC SEPIC Converter for Fast Dynamic Response Using Genetic Algorithm Optimised PI Controller," *IET Circuits, Devices & Systems*, vol. 12, no. 2, pp. 164-174, 2018. [CrossRef] [Google Scholar] [Publisher Link]

[18] M.F. Roslan et al., "Particle Swarm Optimization Algorithm-Based PI Inverter Controller for a Grid-Connected PV System," *PloS One*, vol. 15, no. 12, pp. 1-31, 2020. [CrossRef] [Google Scholar] [Publisher Link]

[19] Mohammed H. Qais, Hany M. Hasanien, and Saad Alghuwainem, "A Grey Wolf Optimizer for Optimum Parameters of Multiple PI Controllers of a Grid-Connected PMSG Driven by Variable Speed Wind Turbine," *IEEE Access*, vol. 6, pp. 44120-44128, 2018. [CrossRef] [Google Scholar] [Publisher Link]

[20] Ali Ahmad et al., "Controller Parameters Optimization for Multiterminal DC Power System Using Ant Colony Optimization," *IEEE Access*, vol. 9, pp. 59910-59919, 2021. [CrossRef] [Google Scholar] [Publisher Link]

[21] Farzam Nejabatkhah et al., "Modeling and Control of a New Three-Input DC–DC Boost Converter for Hybrid PV/FC/Battery Power System," *IEEE Transactions on Power Electronics*, vol. 27, no. 5, pp. 2309-2324, 2012. [CrossRef] [Google Scholar] [Publisher Link]

[22] F. Galea et al., "Design of a High Efficiency Wide Input Range Isolated Cuk DC-DC Converter for Grid Connected Regenerative Active Loads," *World Engineers' Convention*, 2011. [Google Scholar] [Publisher Link]

[23] Patan Javeed et al., "SEPIC Converter for Low Power LED Applications," *Journal of Physics: Conference Series*, vol. 1818, pp. 1-12, 2021. [CrossRef] [Google Scholar] [Publisher Link]

[24] S. Sivarajeswari, and D. Kirubakaran, "Design and Development of Efficient Luo Converters for DC Micro Grid," *The International Journal of Electrical Engineering & Education*, vol. 60, no. 1S, pp. 40-48, 2023. [CrossRef] [Google Scholar] [Publisher Link]